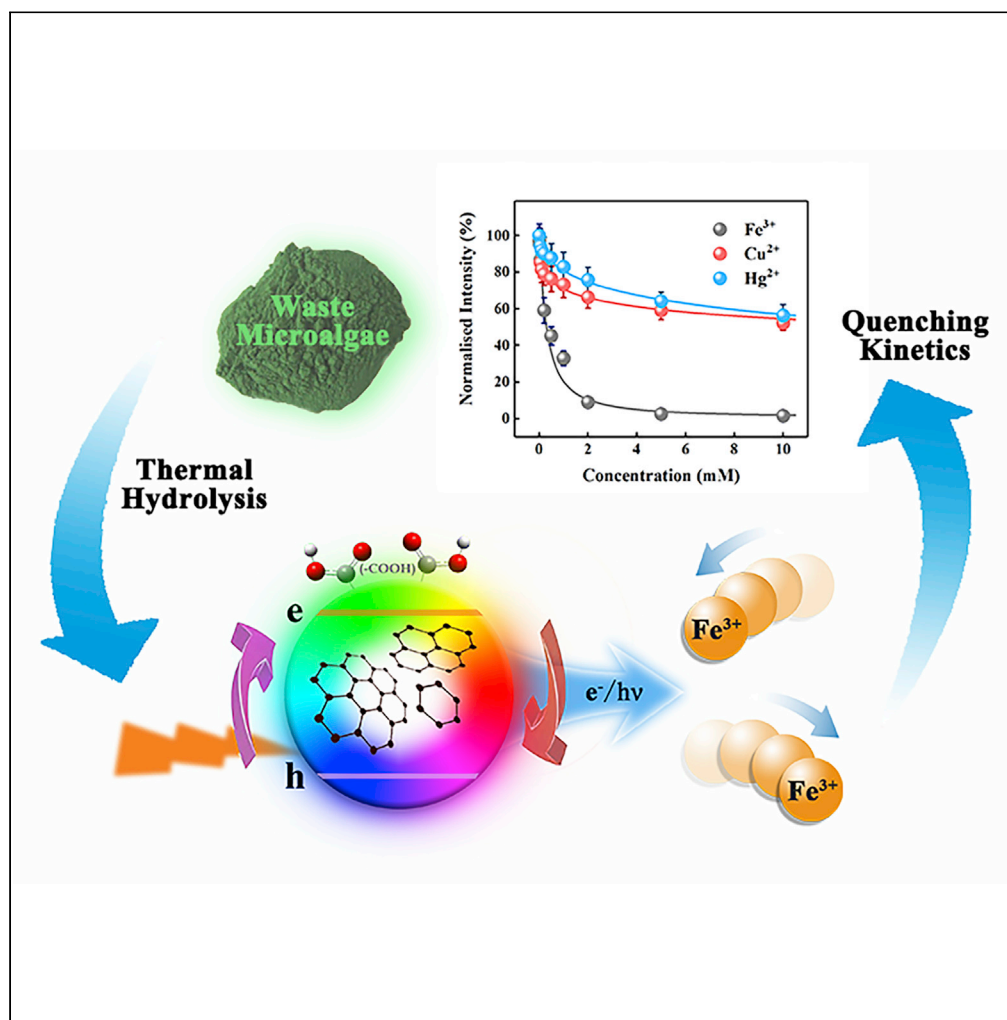


Article

Detecting Ferric Iron by Microalgal Residue-Derived Fluorescent Nanosensor with an Advanced Kinetic Model



Feiyu Liu, Shishu Zhu, Deyang Li, Guanying Chen, Shih-Hsin Ho

stephen6949@hit.edu.cn,
stephen6949@msn.com

HIGHLIGHTS

Microalgal residue-derived carbon dots synthesized by hydrothermal method are introduced

An advanced kinetic model with wide concentration applicability is developed

Waste biomass-derived Fe(III) nanosensor is applied in accurate detection of actual water

Article

Detecting Ferric Iron by Microalgal Residue-Derived Fluorescent Nanosensor with an Advanced Kinetic Model

Feiyu Liu,¹ Shishu Zhu,² Deyang Li,³ Guanying Chen,³ and Shih-Hsin Ho^{1,4,*}

SUMMARY

Biomass-derived carbon quantum dots (CQDs) are attractive to serve as fluorescent nanosensors owing to their superior environmental compatibility and biocompatibility. However, the detection range has been limited, only in partial agreement with the experimental data. Thus, an advanced kinetic model for quantifying the fluorescence quenching over a wide range is on demand. Here, we describe a nanosensor for Fe(III) detection in real waters, which is developed via microalgal residue-derived CQDs with an advanced kinetic model. The multiple-order kinetic model is established to resolve the incoherence of previous models and unveil the entire quenching kinetics. The results show that the detection range of Fe(III) can reach up to 10 mM in the high detection end. The newly obtained kinetic model exhibits satisfactory fittings, clearly elucidating a dynamic quenching mechanism. This work provides a new insight into CQDs-based detection of heavy metals in real water samples by establishing an innovative multiple-order kinetic model.

INTRODUCTION

Contamination of heavy metals in waters possess threats of severe adverse effects on aquatic ecosystem and non-negligible threats to human health (Bansod et al., 2017; Nolan and Lippard, 2008). Although Fe(III) ions regularly participate in various metabolic pathways (such as cellular metabolism and enzyme catalysis) (Gong et al., 2017; Wang et al., 2016b), excessive ingestion of Fe(III) ions into human body would cause certain disorders (i.e., hemochromatosis) (Nguyen et al., 2014). Moreover, high concentration of Fe(III) ions in waters might distort the redox potential of natural aquatic chemistry owing to its fairly strong oxidizing property (Cao et al., 2014; Chan et al., 2019). Therefore, developing high-sensitivity methods with satisfactory accuracy toward Fe(III) ions existing in real water samples is highly required. Previous studies have displayed numerous methods for Fe(III) detection, including atomic absorption spectrometry (Fang et al., 1984), electrochemical analysis (Sadak et al., 2017), liquid chromatography (Kulesza et al., 1987), and inductively coupled plasma atomic emission spectrometry (ICP-AES) (Tangen et al., 2002). However, most of these are operated with high cost and tedious steps that are hard to meet the demand for online actual water survey. As a result, a novel fluorescent nanosensor equipped with nanomaterials as a fluorescence source may be regarded as instrumental in providing a high-throughput method for Fe(III) ion detection.

Benefitting from high quantum yield (QY) and size-tunable emission profiles, quantum dots (QDs) have been considered as the favorable devices for assembling the fluorescent nanosensors for detecting metal ions (Chen and Rosenzweig, 2002). However, extreme toxicity and poor water solubility of popular semiconductor QDs (i.e., CdSe) impeded their application (Gill et al., 2008). Several methodologies were employed to improve their water solubility and for lowering their toxicity, such as surface passivation and coating by silicon oxide films (Sun et al., 2006). But the efficiency of most of these are largely debatable because of the severe fluorescent decay and complex modification procedures (Chao et al., 2013). Instead, CQDs are composed of graphitic microcrystalline cores with sp² hybridization and abundant surface area bearing polar functional groups (Chien et al., 2018). Recent reports have demonstrated that CQDs possess varied application potential owing to the characteristics of low toxicity, high water solubility, environmental compatibility, biocompatibility, and low photobleaching (Lim et al., 2015; Shamsipur et al., 2017; Zhang et al., 2019). The synthetic routes to CQDs are divided into two categories of bottom-up and top-down (Lim

¹State Key Laboratory of Urban Water Resource and Environment, Harbin Institute of Technology, 73 Huanghe Road, Harbin 150090, P. R. China

²School of Environmental Science and Engineering, Sun Yat-Sen University, Guangzhou 510275, P. R. China

³MIT Key Laboratory of Critical Materials Technology for New Energy Conversion and Storage, School of Chemistry and Chemical Engineering & Key Laboratory of Micro-systems and Micro-structures, Ministry of Education, Harbin Institute of Technology, Harbin 150001, P. R. China

⁴Lead Contact

*Correspondence: stephen6949@hit.edu.cn, stephen6949@msn.com
<https://doi.org/10.1016/j.isci.2020.101174>



et al., 2015). Compared with the reported top-down methods (i.e., arc discharge, laser ablation, electrochemical oxidation), the biomass-derived CQDs depending on bottom-up approach could act as low-cost and environment-friendly materials, which have attracted significant interest in the fields of sensing, bioimaging, nanomedicine, photocatalysis, and so on (Gong et al., 2016; Zhang et al., 2019a). Yet, the uncertain mechanism of formation and fluorescence on account of complicated chemical constituents and their structures currently limits the in-depth study on such CQDs.

In addition, although biomass-derived CQDs exhibit advantages of fluorescence quenching-based detection, their specificity is controversial because of the kinetics of fluorescence quenching still being dubious. The Stern-Volmer (SV) equation is a basic theoretical kinetic model describing the dynamic quenching mechanism of fluorescence quenching-based sensors. However, this model cannot be well-fitted to the experimental results as the quencher concentration increased, presenting the progressively larger deviation in high quencher concentration condition (Song et al., 2014). Following this, some resultant kinetic models were developed to adapt the misfits such as partial fitting or dual-model matching utilizing different equations as well as different parameters (Liu et al., 2012; Qi et al., 2018; Yang et al., 2017). For instance, Plácido et al. (2019) employed a modified kinetic model by converting the concentration coordinate to the logarithm of concentration to further fit the experimental data. However, these reported kinetic models were established merely by the mathematical fitting of experimental results, which are hard to satisfy different quenching systems, and thus hinder the understanding of actual quenching mechanisms. Various previously reported quenching systems and their corresponding resultant kinetic models are listed in Table S1.

The phycocyanin-extracted microalgal residue is considered as a hazardous waste biomass consisting of large amounts of inorganic salts (around 30% of the dry cell weight), causing a tremendous disposal risk. Luckily, the salts present in microalgal residue may be conducive to its structural decomposition and consequent the formation of CQDs (Rizzo et al., 2018). Thus, we herein fabricated an innovative Fe(III) nanosensor from phycocyanin-extracted microalgal residue through a hydrothermal method. This real-water applicable fluorescence quenching-based detection method was then established by formulating an advanced kinetic model. With the emergence of the multiple-order kinetic model, the mathematical operation was systematically formulated and concluded. Several typical fluorescence quenching conditions also showed decent fitting results with the advanced kinetic model. Furthermore, the quenching mechanisms were eventually established via quenching-recovery experiment and fluorescence lifetime measurement under different quencher concentrations. As a result, this work clearly demonstrates that the as-prepared CQDs nanosensor may be a powerful tool for precisely detecting Fe(III) and fashions a convincing advanced kinetic model together with revealing the corresponding mechanism for maximizing its application potential.

RESULTS AND DISCUSSION

Properties of the Obtained CQDs

As shown in Figure 1A, the quasi-spherical and monodispersed microalgal residue-derived CQDs were observed. Based on the auto-measurement of size distribution, the average Feret diameter of CQDs was found to be 8.5 ± 2.2 nm, which is similar to the previous reports (Ramanan et al., 2016). The high-resolution TEM image of single CQD was shown in Figure S1 with the lattice parameter of about 0.24 nm, representing the (1120) lattice fringe of graphene (Yang et al., 2017). As observed from the full range of XPS survey spectrum (Figure S2), the surface of CQDs was mostly composed of carbon and oxygen atoms. Signals of Ca and Cl atoms were also found from the inherent minerals in biomass precursors (Hao et al., 2017). The signal of C 1s (Figure 1B) could be de-convoluted as three characteristic peaks at 284.7, 285.9, and 288.3 eV, attributing to C-C/C=C, C-O/C-O-C, and C=O groups, respectively (Lu et al., 2012). In the O 1s spectrum (Figure 1C), the de-convoluted three peaks at 531.1, 531.9, and 533.0 eV could refer to C-OO, C=O, and C-O/C-O-C moieties, respectively (Liu et al., 2016). The Fourier transform infrared (FTIR) spectrum of CQDs (Figure 1D) was recorded to recognize the surface functionalization. A broad absorption peak from 3,700 to 2,700 cm^{-1} was assigned to C-H and the -OH stretching vibrations observed within CQDs, conforming to the previous study that demonstrated abundant existence of -OH on the edges of CQDs (Cayuela et al., 2016). Other surface oxygenic functional groups could be confirmed from the absorptions at 1,720 cm^{-1} and 1,230 cm^{-1} , respectively, which are attributed to C=O and C-O groups (Guo et al., 2015). The band at 1,400 cm^{-1} revealed that the aromatics C-C stretching vibration existed as the indicator of graphited carbon matrix in CQDs (Trang Thi and Park, 2016). In addition, the carbonization peak

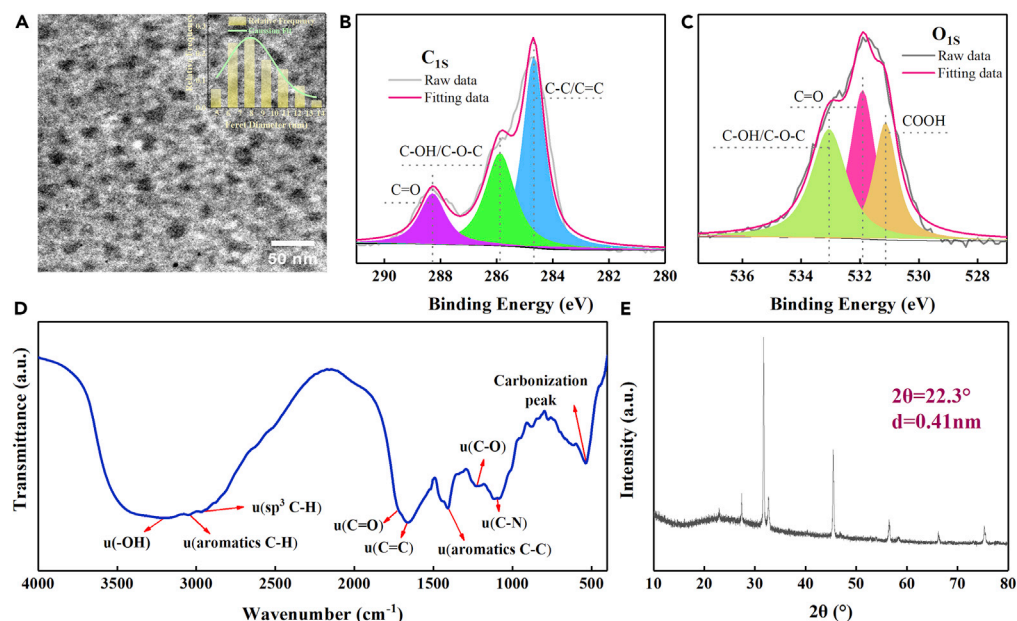


Figure 1. Structural Characterization of CQDs

(A) TEM images and size distribution (scale bar, 1.5 cm).

(B) XPS spectra (C1s peaks).

(C) XPS spectra (O1s peaks).

(D) FTIR spectra.

(E) XRD patterns of CQDs.

See also [Figures S1](#) and [S2](#).

appeared at about 530 cm^{-1} (Ramanan et al., 2016). In the XRD pattern (Figure 1E), the peak centered at 2θ of 22.3° was consistent with (002) lattice facet of graphitic crystalline structure (Ramanan et al., 2016). It was noted that the lattice spacing (0.42 nm) was larger than that of bulk graphite (0.33 nm), indicating the turbostratic phase of CQDs, which incorporated micro-crystallization as well as amorphous carbon (Tian et al., 2009). Other sharp peaks in the XRD pattern stand for crystalline CaCl_2 introduced from microalgal residue. Therefore, it can be concluded that the obtained CQDs were minor-sized turbostratic carbonaceous dots constituting the graphited core and abundant sp^3 oxygen-containing groups on the edges.

The excitation-dependent emission map (Figure 2A) exhibits three photoluminescence (PL) peaks. The occurrence of PL peaks resulted from the transfer and recombination of excited electrons on three fluorescent active centers between the graphited core and surface of CQDs (Kumar Thiyagarajan et al., 2016). The visual photophysical information is represented by virtue of PL and photoluminescence excitation (PLE) spectra (Figure 2B). A blue fluorescence emission appeared from the CQDs under 355-nm UV irradiation. Moreover, two peaks in PLE spectrum at 300 and 355 nm indicated core and surface absorption, respectively. The absorption at 280 nm indicates the π - π^* transition in aromatic C=C bond, whereas the absorption at 330 nm is attributed to n - π^* transition in C-O and C=O bonds (Figure 2B). These results suggest the behavior of electron transfer followed the adsorption pattern of the core and surface of CQDs, respectively (Luo et al., 2009). Similar to most carbon-based nanomaterials, the microalgal residue-derived CQDs displayed the excitation-dependent emissions (Figure 2C) in the range of 260- to 380-nm excitation wavelength. Centered at 435 nm, the CQDs displayed the strongest blue fluorescence when excited at 355 nm, which was selected to act as the preferred experimental parameter of following quenching and detection tests.

Based on concentration-dependent PL intensity (Figure S3), the quantum yield (Φ) of CQDs was found to be 7.7% against the reference of quinine sulfate in 0.1 M H_2SO_4 . The obtained Φ demonstrated that the fluorescence was mostly generated by CQDs instead of fluorescent molecule. The PL decay behavior of CQDs was quantified by a time-correlated single-photon counting technique, as shown in Figure 2D. As fitted by the biexponential decay equation (Black et al., 2017), the PL lifetime was dominated by the decay

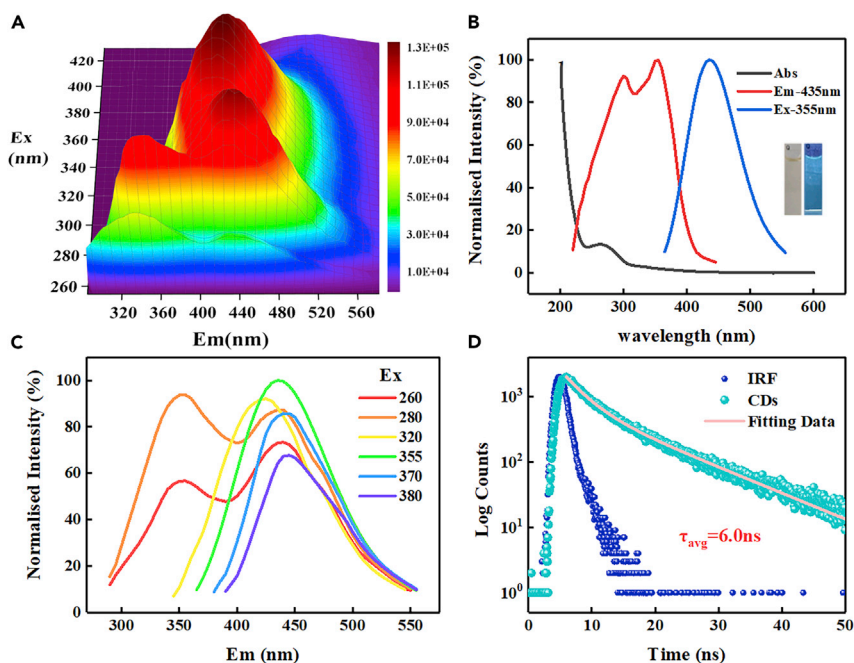


Figure 2. Optical Properties of CQDs

- (A) Excitation-dependent emission map.
 (B) UV-vis, PL, and PLE spectra of CQDs.
 (C) PL spectra at different excitation wavelengths (260–380 nm).
 (D) PL decay curve at 355 nm.

See also [Figures S3](#) and [S4](#).

parameter of 5.96 ns as along with a small contribution from that of 10.93 ns. The average PL lifetime calculated as 6.0 ns was represented as the reference in this study, which is similar to the previous reported biomass-derived CQDs (6.87 ns) (Li et al., 2015). As shown in [Figure S4](#), CQDs exhibited high fluorescence stability under long-period UV irradiation, high ionic strength, and a wide pH range. Specifically, the decay of fluorescent intensity in acidic (pH less than 3) or alkaline (pH more than 11) environments may be attributed to the changes in interfacial structures on CQDs. In addition, CQDs maintained the strongest emission while dispersed in water, compared with the ones in lower-polarity organic solvents ([Figure S4A](#)). Such properties of CQDs may be beneficial for working as a nanosensor in real water.

Label-free Detection of Fe(III)

To evaluate the selectivity of the CQDs as a nanosensor toward Fe(III), the most common ions existing in natural aquatic environments (i.e., Na^+ , K^+ , CO_3^{2-} , NO_3^-) were also employed in addition to Fe(III), to quench the suspension containing 100 mg L^{-1} CQDs ([Figure 3A](#)). With the involvement of Fe(III), the highest quenching rate of 84% was obtained. [Figure 3B](#) further indicates the anti-jamming capability of Fe(III) detection by microalgal residue-derived CQDs nanosensor, showing that no obvious changes in PL intensities were present after addition of various high-concentration (2 mM) cations to the Fe(III) quenching, thus indicating that the CQDs have great selectivity without interference, for Fe(III) detection.

The Fe(III)-induced quenching behavior of CQDs was explored by a stepwise-quenching method of adding Fe(III) ions ranging from 0.01 to 10 mM ([Figure 3C](#)). Before complete quenching, the quenching effect exponential heightened with the increase in the concentration of quencher. When fitted only by traditional static or dynamic kinetic models as reported in a previous study (Liang et al., 2016), the calculated curve seemed to be partially corresponding to the experimental data. In view of the kinetic model to better describe the corresponding chemical reaction (Wang et al., 2016a), the order of i was then introduced to establish the multiple-order quenching kinetic model for absolutely fitting the experimental data. Taking logarithm of concentration as the x axis and the logarithm of $F_0/F-1$ as the y axis, the linear fitting of quenching kinetics was found to have an excellent correlation coefficient (R^2) of 0.9810 ([Figure 3C](#)). These results further reveal

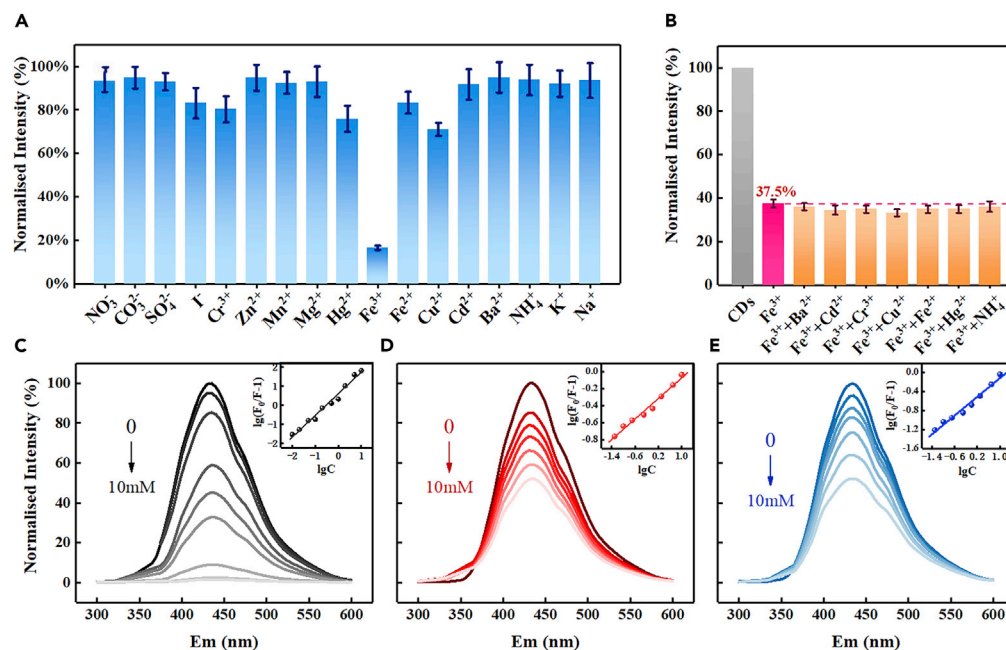


Figure 3. Application of Fluorescence Nanosensor

(A) Influence of different ions (1 mM) on the PL intensity change of CQDs. (Data are represented as mean \pm SEM.)

(B) Cation interference (1 mM) on Fe(III) quenching of CQDs. (Data are represented as mean \pm SEM.)

(C) Fluorescence quenching responses of the CQDs (100 mg/L) with Fe(III).

(D) Fluorescence quenching responses of the CQDs (100 mg/L) with Cu(II).

(E) Fluorescence quenching responses of the CQDs (100 mg/L) with Hg(II).

See also [Figures S5 and S6](#), [Tables S1 and S2](#).

the quenching constant (K_{SV}) to be $3.94 \times 10^3 \text{ L} \cdot \text{mol}^{-1}$ and the quenching order (i) to be 1.14, suggesting a high quenching efficiency of Fe(III) on the CQDs. From the standard curve, the limit of detection (LOD) for this method was estimated to be 1.67 μM , corresponding to 93.4 ppb. It clearly indicates that the Fe(III) detection by the as-prepared CQDs nanosensor exhibits greater merits along with simplicity, high sensitivity, and fast response.

To examine the practical application potential of the CQDs nanosensor, tap water, river water, and municipal wastewater with different water qualities were chosen as the real-world water samples. Spiked with the Fe(III) ions at concentrations of 0, 0.15, 0.30, and 0.60 mg L^{-1} (in keeping with standard China policy of 0.3 mg L^{-1} in drinking water), the reliable quantification of Fe(III) concentrations in the samples was done by ICP-AES, along with calculating the corresponding quenching kinetics for comparison. ICP-AES is noticed as a reliable method for highly accurate heavy metals detection, which is generally selected as the criterion in evaluating the applicability of newly ions detectors ([Asfaw and Wibetoe, 2005](#)). As shown in [Table 1](#), the nanosensor-detected concentrations of Fe(III) exhibited a good agreement with the values determined by ICP-AES, which performed nearly 100% recovery rate under different standard concentration. Moreover, the standard deviation was accepted for a detection method of water samples. The results suggest that the fluorescent nanosensor CQDs can work in real water samples as a tool to establish a practical and promising method for the Fe(III).

Application of Multiple-Order Quenching Kinetic Model

As mentioned above, the multiple-order kinetic model obtained by introducing a new parameter in molecular-level fluorescence quenching processes explained the previous models by partial or two-stage fitting. To ascertain the applicability of such multiple-order kinetics, four fluorescence quenching systems with the diverse quenchers or fluorescent sources were employed. Initially, the Cu(II) and Hg(II) with quenching efficiencies lower than Fe(III) were selected to quench the CQDs ([Figure 3A](#)). [Figures 3D and 3E](#) showed the quenching PL curves and the linear fitting of kinetics based on the quenching processes by the solutions having concentrations of 0.05–10 mM of Cu(II) or Hg(II). The multiple-order quenching kinetics model fitted

Sample	Fe(III) Addition (mg/L)	Proposed Method (mg/L, Mean ^a ± SD ^b)	ICP-AES (mg/L, Mean ± SD)
Tap water 1	0	0.011 ± 0.003	0.012 ± 0.002
Tap water 2	0.15	0.162 ± 0.021	0.162 ± 0.005
Tap water 3	0.30	0.309 ± 0.040	0.311 ± 0.010
Tap water 4	0.60	0.613 ± 0.089	0.615 ± 0.023
Songhua river water 1	0	0.143 ± 0.019	0.140 ± 0.004
Songhua river water 2	0.15	0.297 ± 0.041	0.294 ± 0.009
Songhua river water 3	0.30	0.440 ± 0.077	0.447 ± 0.014
Songhua river water 4	0.60	0.750 ± 0.108	0.749 ± 0.021
Municipal wastewater 1	0	0.065 ± 0.010	0.064 ± 0.004
Municipal wastewater 2	0.15	0.210 ± 0.018	0.210 ± 0.013
Municipal wastewater 3	0.30	0.371 ± 0.043	0.365 ± 0.021
Municipal wastewater 4	0.60	0.673 ± 0.092	0.670 ± 0.033

Table 1. Fe(III) Detection in Different Waters Based on Standard Recovery Method

^aMean of three determinations.

^bStandard deviation.

well with the experimental data with the R^2 of 0.9808 (Cu(II)) and 0.9773 (Hg(II)), in spite of the incomplete quenching efficiency. These results indicate that this newly established multiple-order kinetics model could be fitted well to different quenchers within CQDs nanosensors. The nonlinear kinetics fitting of fluorescent intensity toward quencher concentration by three different ion quenchers is shown in Figure S5. The fitting of nonlinear curves revealed an exponential-like decay function at the initial stages with the rapid decline in intensity. The linear or two-stage linear model in previous studies (Guan et al., 2017) interpreted the kinetic process only in partial range of the quencher concentration. However, the multiple-order kinetics model could further account for the entire quenching process and the complicated quenching mechanisms with a mathematical reality. Consequently, the higher quenching efficiency in Fe(III) could be attributed to the lower values of the key kinetic parameters of K_{SV} and i (Table S2).

To assess the application potential of the established multiple-order kinetics model, the common fluorescent compound MB was used based on its wide application as a chemical indicator and biological stain. Moreover, MB gave off a similar PL spectrum to the as-prepared CQDs because of its thiophenylamine structure (Kiwi et al., 1999) (Figure S6A). Thus, the kinetic behavior of MB quenching could be compared to the CQDs fluorescent quenching. As shown in Figure S6B, an excellent fitting of Fe(III)-induced quenching of the MB system ($R^2 = 0.9967$) by the multiple-order model was observed. A lower quenching efficiency of 60% in MB than that in case of CQDs resulted from the differences in K_{SV} and i values (Figure S6C). These results could summarize the good fitting of the multiple-order kinetic model with the experimental results in fluorescent quenching systems regardless of the fluorescent substances and quenchers used therein. Compared with the applicable linear or SV model with partial fitting, the multiple-order model can provide a more accurate theoretical kinetics to better describe the fluorescent quenching-based detection. More importantly, it is worthwhile to consider the physical meanings of K_{SV} and i together with the further mechanisms involved.

Quenching Mechanism

The fluorescent quenching mechanisms involving the interactions between CQDs and ionized quenchers were carefully explored. A previous study has indicated that Fe(III) ions could bond with the superficial phenolic hydroxyl groups of CQDs by means of chelation interaction. Therein, the quenching of the fluorescence may occur by hindering the electron transfer (Li et al., 2018). To verify the above hypothesis, a fluorescent quenching recovery experiment was executed. Owing to high binding affinity with Fe(III), EDTA, citric acid, and NH₃ were then selected as the strong complexing agents to spike the CQDs during the

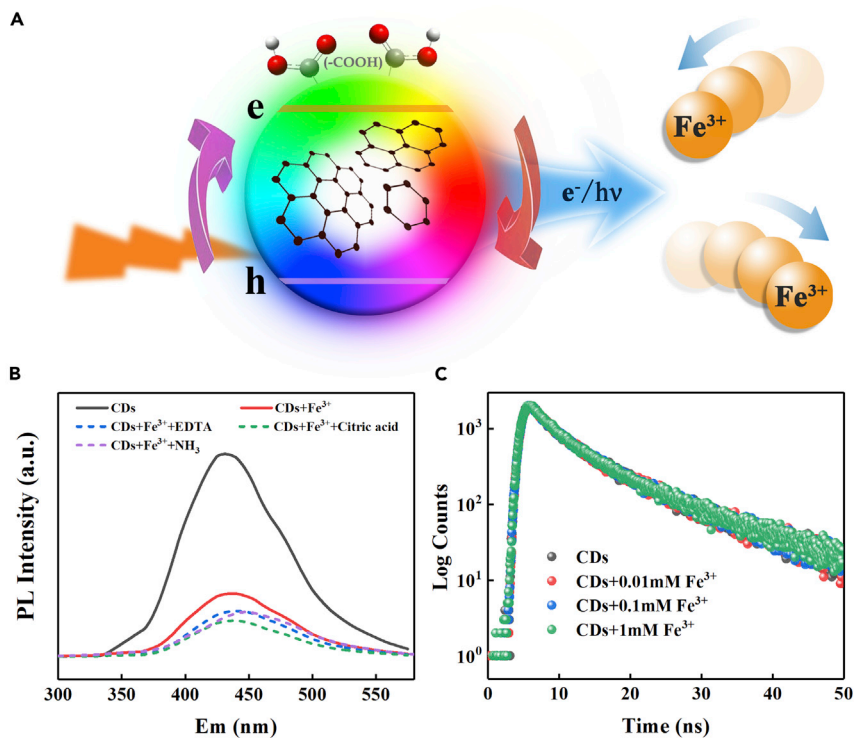


Figure 4. Fluorescence Quenching Mechanism

(A) Schematic diagram of Fe(III) dynamic quenching on CQDs.

(B) Fluorescence recovery of Fe(III) quenched CQDs by different complexing agents.

(C) PL decay curve of CQDs quenched by different Fe(III) concentrations.

See also [Figure S7](#).

quenching processes utilizing 1 mM Fe(III) ions to verify whether the complexing action happened between Fe(III) ions and CQDs. If the CQDs were indeed quenched by chelation interaction, which changed the inherent property of CQDs, the complexing agents with stronger binding ability would compete with the sites on CQDs for the Fe(III) ions and lead to the recovery of fluorescence within CQDs. As shown in [Figure 4B](#), a reduction in fluorescent intensity instead of the expected recovery was observed on adding the complexing agents. The tendency adverse to the hypothesis of static-quenching process may have resulted from the formation of Fe(III)-chelate, which could improve the ionic strength (Cui et al., 2017). Therefore, this phenomenon indicates that the interaction between Fe(III) and CQDs did not follow the pattern of static quenching, which may proceed by altering the inherent chemical surface structure of CQDs. In addition, to examine whether Fe(III) affected the surface state of CQDs, the study on zeta-potential variations upon changing the pH was carried out (Berg et al., 2009). [Figure S7](#) shows a similar variation trend and an isoelectric point (IEP) no matter whether other quenching ions were introduced or not. Accordingly, the quenching of CQDs by Fe(III) may be a dynamic collision process, which does not alter the inherent property of CQDs. Previous studies have demonstrated that the dynamic quenching could be attributed to the interaction of the quencher with the excited states of CQDs, which would not impact the fluorescence lifetime of CQDs (Liang et al., 2016). To directly validate the dynamic quenching process, we further employed the PL decay curves to observe the variation in fluorescence lifetime after spiking with different concentrations of Fe(III) ions. The measured PL decay curves barely displayed any difference under different concentrations of Fe(III) ions ([Figure 4C](#)). The fluorescence lifetime was regarded as an effective indicator for the extra-nuclear electrons generating fluorescence due to the transition and recombination among themselves (Liang et al., 2016). As stated in [Equation S4 \(Transparent Methods\)](#), the variance of fluorescence lifetime depended on the changes in intrinsic transition rate k_f and the summation of all the non-radiative jump rates $\sum k_i$. Correspondingly, the dynamic quenching process was established as a concentration-related transition parameter, which cannot raise any change in fluorescence lifetime (Dong et al., 2012; Ju and Chen, 2014). Thus, we here conclude that the quenching of CQDs by Fe(III) ions followed the mechanism of dynamic quenching. The aforementioned direct dynamic-quenching process is graphically displayed in

Figure 4A. The CQDs with a graphitic core and carboxylic acid surface could absorb high-wavelength light and thus cause the electron transition. The excited CQDs interacted with mobile Fe(III) ions by electron or photon transfer, and fluorescent quenching occurred according to the non-radiative electron-hole recombination mechanism. The interaction of excited electrons and ions should be further studied to develop more selective and sensitive fluorescent nanosensors, along with exploring the actual quenching mechanisms based on the advanced kinetics model.

Conclusion

In the study, we employed the microalgal residue-derived CQD as Fe(III) nanosensor. The CQD synthesized by a facile hydrothermal process exhibited a mass yield of 33.4% and quantum yield of 7.7%. Without further passivation or modification, the obtained CQD was found to be a highly efficient Fe(III) nanosensor. The “turn-off” fluorescent detection method with sensitivity and wide-concentration applicability has been developed by the advanced kinetic model, which was approved in different fluorescent quenching systems. Moreover, the lifetime-constant dynamic-quenching process was confirmed and may be attributed to the electron or photon transfer from excited surface of CQDs to the mobile Fe(III) ions. The study not only provided an eco-friendly approach of manufacturing CQDs by low-cost biomass waste but also offered the valuable information of promising application of Fe(III) ions detection for actual water samples by CQDs. Most importantly, the developed advanced kinetic model provides a new insight for fluorescence quenching kinetics and mechanism in bioimage and fluorescent nanosensor.

Limitations of the Study

This work established a microalgae residue-derived fluorescence nanosensor for Fe(III) detection with an advanced kinetic model. The application of the sensor was limited in water samples. More application scenarios (i.e., cell imaging) could be considered in the future study. Moreover, by introducing the reaction order parameter i , the advanced kinetic model exhibits satisfactory fittings over a wide detection range. But the physical significance and influence factor of the parameter i were indistinct. For extensive application of the advanced model, more effort should be adopted in terms of fluorescence quenching mechanism.

Resource Availability

Lead Contact

Further information and requests for resources and reagents should be directed to and will be fulfilled by the Lead Contact, Shih-Hsin Ho (stephen6949@hit.edu.cn).

Materials Availability

All unique/stable reagents generated in this study are available from the Lead Contact without restriction.

Data and Code Availability

All relevant data are available from the corresponding author (stephen6949@hit.edu.cn) upon reasonable request.

METHODS

All methods can be found in the accompanying [Transparent Methods supplemental file](#).

SUPPLEMENTAL INFORMATION

Supplemental Information can be found online at <https://doi.org/10.1016/j.isci.2020.101174>.

ACKNOWLEDGMENTS

This work was financially supported by the National Natural Science Foundation of China (No. 5181101550) and the Project of Thousand Youth Talents (No. AUGA2160100917).

AUTHOR CONTRIBUTIONS

F.L.: Conceptualization, Resources, Formal analysis, Writing - Original Draft. S.-H.H.: Conceptualization, Funding acquisition, Writing - Review & Editing. S.Z.: Writing - Review & Editing. D.L.: Resources. G.C.: Writing - Review & Editing.

DECLARATION OF INTERESTS

The authors declare no competing financial interest.

Received: March 10, 2020

Revised: May 5, 2020

Accepted: May 13, 2020

Published: June 26, 2020

REFERENCES

- Asfaw, A., and Wibetoe, G. (2005). Direct analysis of beer by ICP-AES: a very simple method for the determination of Cu, Mn and Fe. *Microchim. Acta* 152, 61–68.
- Bansod, B., Kumar, T., Thakur, R., Rana, S., and Singh, I. (2017). A review on various electrochemical techniques for heavy metal ions detection with different sensing platforms. *Biosens. Bioelectron.* 94, 443–455.
- Berg, J.M., Romoser, A., Banerjee, N., Zebda, R., and Sayes, C.M. (2009). The relationship between pH and zeta potential of ~ 30 nm metal oxide nanoparticle suspensions relevant to in vitro toxicological evaluations. *Nanotoxicology* 3, 276–283.
- Black, L.E., Cavalli, A., Verheijen, M.A., Haverkort, J.E.M., Bakkers, E.P.A.M., and Kessels, W.M.M. (2017). Effective surface passivation of InP nanowires by atomic-layer-deposited Al₂O₃ with POx interlayer. *Nano Lett.* 17, 6287–6294.
- Cao, H., Chen, Z., Zheng, H., and Huang, Y. (2014). Copper nanoclusters as a highly sensitive and selective fluorescence sensor for ferric ions in serum and living cells by imaging. *Biosens. Bioelectron.* 62, 189–195.
- Cayuela, A., Carrillo-Carrion, C., Soriano, M.L., Parak, W.J., and Valcarcel, M. (2016). One-step synthesis and characterization of N-doped carbon nanodots for sensing in organic media. *Anal. Chem.* 88, 3178–3185.
- Chan, K.K., Yang, C., Chien, Y.-H., Panwar, N., and Yong, K.-T. (2019). A facile synthesis of label-free carbon dots with unique selectivity-tunable characteristics for ferric ion detection and cellular imaging applications. *New J. Chem.* 43, 4734–4744.
- Chao, M.-R., Chang, Y.-Z., and Chen, J.-L. (2013). Hydrophilic ionic liquid-passivated CdTe quantum dots for mercury ion detection. *Biosens. Bioelectron.* 42, 397–402.
- Chen, Y.F., and Rosenzweig, Z. (2002). Luminescent CdS quantum dots as selective ion probes. *Anal. Chem.* 74, 5132–5138.
- Chien, Y.H., Chan, K.K., Yap, S.H.K., and Yong, K.T. (2018). NIR-responsive nanomaterials and their applications; upconversion nanoparticles and carbon dots: a perspective. *J. Chem. Technol. Biotechnol.* 93, 1519–1528.
- Cui, X., Wang, Y., Liu, J., Yang, Q., Zhang, B., Gao, Y., Wang, Y., and Lu, G. (2017). Dual functional N- and S-co-doped carbon dots as the sensor for temperature and Fe³⁺ ions. *Sens. Actuators B Chem.* 242, 1272–1280.
- Dong, Y.Q., Wang, R.X., Li, G.L., Chen, C.Q., Chi, Y.W., and Chen, G.N. (2012). Polyamine-Functionalized carbon quantum dots as fluorescent probes for selective and sensitive detection of copper ions. *Anal. Chem.* 84, 6220–6224.
- Fang, Z., Růžicka, J., and Hansen, E.H. (1984). An efficient flow-injection system with on-line ion-exchange preconcentration for the determination of trace amounts of heavy metals by atomic absorption spectrometry. *Anal. Chim. Acta* 164, 23–39.
- Gill, R., Zayats, M., and Willner, I. (2008). Semiconductor quantum dots for bioanalysis. *Angew. Chem. Int. Ed.* 47, 7602–7625.
- Gong, X.J., Li, Z.B., Hu, Q., Zhou, R.X., Shuang, S.M., and Dong, C. (2017). N,S,P Co-doped carbon nanodot fabricated from waste microorganism and its application for label-free recognition of manganese(VII) and l-ascorbic acid and AND logic gate operation. *ACS Appl. Mater. Interfaces* 9, 38761–38772.
- Gong, Y., Yu, B., Yang, W., and Zhang, X. (2016). Phosphorus, and nitrogen co-doped carbon dots as a fluorescent probe for real-time measurement of reactive oxygen and nitrogen species inside macrophages. *Biosens. Bioelectron.* 79, 822–828.
- Guan, Y.-F., Huang, B.-C., Qian, C., and Yu, H.-Q. (2017). Quantification of humic substances in natural water using nitrogen-doped carbon dots. *Environ. Sci. Technol.* 51, 14092–14099.
- Guo, R., Zhou, S., Li, Y., Li, X., Fan, L., and Voelcker, N.H. (2015). Rhodamine-Functionalized graphene quantum dots for detection of Fe³⁺ in cancer stem cells. *ACS Appl. Mater. Interfaces* 7, 23958–23966.
- Hao, R., Zhang, Y., Wang, Z., Li, Y., Yuan, B., Mao, X., and Zhao, Y. (2017). An advanced wet method for simultaneous removal of SO₂ and NO from coal-fired flue gas by utilizing a complex absorbent. *Chem. Eng. J.* 307, 562–571.
- Ju, J., and Chen, W. (2014). Synthesis of highly fluorescent nitrogen-doped graphene quantum dots for sensitive, label-free detection of Fe (III) in aqueous media. *Biosens. Bioelectron.* 58, 219–225.
- Kiwi, J., Denisov, N., and Nadochenko, V. (1999). Interfacial electron transfer induced by light in methylene blue incorporated in nafion membranes. *Laser kinetic spectroscopy. J. Phys. Chem. B* 103, 9141–9148.
- Kulesza, P.J., Brajter, K., and Dabek-Zlotorzynska, E. (1987). Application of chelate-forming resin and modified glassy carbon electrode for selective determination of iron(III) by liquid chromatography with electrochemical detection. *Biosens. Bioelectron.* 59, 2776–2780.
- Kumar Thiyagarajan, S., Raghupathy, S., Palanivel, D., Raji, K., and Ramamurthy, P. (2016). Fluorescent carbon nano dots from lignite: unveiling the impeccable evidence for quantum confinement. *Phys. Chem. Chem. Phys.* 18, 12065–12073.
- Li, L., Yu, B., and You, T. (2015). Nitrogen and sulfur co-doped carbon dots for highly selective and sensitive detection of Hg (II) ions. *Biosens. Bioelectron.* 74, 263–269.
- Li, Y., Ren, J., Sun, R., and Wang, X. (2018). Fluorescent lignin carbon dots for reversible responses to high-valence metal ions and its bioapplications. *J. Biomed. Nanotechnol.* 14, 1543–1555.
- Liang, Z., Kang, M., Payne, G.F., Wang, X., and Sun, R. (2016). Probing energy and electron transfer mechanisms in fluorescence quenching of biomass carbon quantum dots. *ACS Appl. Mater. Interfaces* 8, 17478–17488.
- Lim, S.Y., Shen, W., and Gao, Z.Q. (2015). Carbon quantum dots and their applications. *Chem. Soc. Rev.* 44, 362–381.
- Liu, S., Tian, J., Wang, L., Zhang, Y., Qin, X., Luo, Y., Asiri, A.M., Al-Youbi, A.O., and Sun, X. (2012). Hydrothermal treatment of grass: a low-cost, green route to nitrogen-doped, carbon-rich, photoluminescent polymer nanodots as an effective fluorescent sensing platform for label-free detection of Cu(II) ions. *Adv. Mater.* 24, 2037–2041.
- Liu, X.L., Jiang, H., Ye, J., Zhao, C.Q., Gao, S.P., Wu, C.Y., Li, C.H., Li, J.C., and Wang, X.M. (2016). Nitrogen-doped carbon quantum dot stabilized magnetic iron oxide nanoprobe for fluorescence, magnetic resonance, and computed tomography triple-modal in vivo bioimaging. *Adv. Funct. Mater.* 26, 8694–8706.
- Lu, Y.Z., Jiang, Y.Y., Wei, W.T., Wu, H.B., Liu, M.M., Niu, L., and Chen, W. (2012). Novel blue light emitting graphene oxide nanosheets fabricated by surface functionalization. *J. Mater. Chem.* 22, 2929–2934.
- Luo, Z.T., Lu, Y., Somers, L.A., and Johnson, A.T.C. (2009). High yield preparation of macroscopic graphene oxide membranes. *J. Am. Chem. Soc.* 131, 898–899.
- Nguyen, T.D., Labed, A., El Zein, R., Lavandier, S., Bedu, F., Ozerov, I., Dallaporta, H., Raimundo, J.-M., and Charrier, A.M. (2014). A field effect transistor biosensor with a γ -pyrone derivative engineered lipid-sensing layer for ultrasensitive

- Fe³⁺ ion detection with low pH interference. *Biosens. Bioelectron.* **54**, 571–577.
- Nolan, E.M., and Lippard, S.J. (2008). Tools and tactics for the optical detection of mercuric ion. *Chem. Rev.* **108**, 3443–3480.
- Plácido, J., Bustamante-López, S., Meissner, K.E., Kelly, D.E., and Kelly, S.L. (2019). Microalgae biochar-derived carbon dots and their application in heavy metal sensing in aqueous systems. *Sci. Total Environ.* **656**, 531–539.
- Qi, H., Teng, M., Liu, M., Liu, S., Li, J., Yu, H., Teng, C., Huang, Z., Liu, H., and Shao, Q. (2018). Biomass-derived nitrogen-doped carbon quantum dots: highly selective fluorescent probe for detecting Fe³⁺ ions and tetracyclines. *J. Colloid. Interface Sci.* **539**, 332–341.
- Ramanan, V., Thiyagarajan, S.K., Raji, K., Suresh, R., Sekar, R., and Ramamurthy, P. (2016). Outright green synthesis of fluorescent carbon dots from eutrophic algal blooms for in vitro imaging. *ACS Sustain. Chem. Eng.* **4**, 4724–4731.
- Rizzo, C., Arcudi, F., Đorđević, L., Dintcheva, N.T., Noto, R., D’Anna, F., and Prato, M. (2018). Nitrogen-Doped carbon nanodots-ionogels: preparation, characterization, and radical scavenging activity. *ACS Nano* **12**, 1296–1305.
- Sadak, O., Sundramoorthy, A.K., and Gunasekaran, S. (2017). Highly selective colorimetric and electrochemical sensing of iron (III) using Nile red functionalized graphene film. *Biosens. Bioelectron.* **89**, 430–436.
- Shamsipur, M., Barati, A., and Karami, S. (2017). Long-wavelength, multicolor, and white-light emitting carbon-based dots: achievements made, challenges remaining, and applications. *Carbon* **124**, 429–472.
- Song, Y., Zhu, S., Xiang, S., Zhao, X., Zhang, J., Zhang, H., Fu, Y., and Yang, B. (2014). Investigation into the fluorescence quenching behaviors and applications of carbon dots. *Nanoscale* **6**, 4676–4682.
- Sun, Y.-P., Zhou, B., Lin, Y., Wang, W., Fernando, K.A.S., Pathak, P., Meziani, M.J., Harruff, B.A., Wang, X., Wang, H., et al. (2006). Quantum-sized carbon dots for bright and colorful photoluminescence. *J. Am. Chem. Soc.* **128**, 7756–7757.
- Tangen, G., Wickstrom, T., Lierhagen, S., Vogt, R., and Lund, W. (2002). Fractionation and determination of aluminum and iron in soil water samples using SPE cartridges and ICP-AES. *Environ. Sci. Technol.* **36**, 5421–5425.
- Tian, L., Ghosh, D., Chen, W., Pradhan, S., Chang, X., and Chen, S. (2009). Nanosized carbon particles from natural gas soot. *Chem. Mater.* **21**, 2803–2809.
- Trang Thi, B., and Park, S.-Y. (2016). A carbon dot-hemoglobin complex-based biosensor for cholesterol detection. *Green. Chem.* **18**, 4245–4253.
- Wang, L., Li, B., Xu, F., Shi, X., Feng, D., Wei, D., Li, Y., Feng, Y., Wang, Y., and Jia, D. (2016a). *Biosens. Bioelectron.* **79**, 1–8.
- Wang, Y., Meng, H., Jia, M.Y., Zhang, Y., Li, H., and Feng, L. (2016b). Intraparticle FRET of Mn(II)-doped carbon dots and its application in discrimination of volatile organic compounds. *Nanoscale* **8**, 17190–17195.
- Yang, R., Guo, X., Jia, L., Zhang, Y., Zhao, Z., and Lonshakov, F. (2017a). Green preparation of carbon dots with mangosteen pulp for the selective detection of Fe³⁺ ions and cell imaging. *Appl. Surf. Sci.* **423**, 426–432.
- Yang, S., Li, W., Ye, C., Wang, G., Tian, H., Zhu, C., He, P., Ding, G., Xie, X., and Liu, Y. (2017b). C₃N-A 2D Crystalline, Hole-Free, Tunable-Narrow-Bandgap Semiconductor with Ferromagnetic Properties. *Adv. Mater.* **29**, 1605625.
- Zhang, Q., Deng, S., Liu, J., Zhong, X., He, J., Chen, X., Feng, B., Chen, Y., and Ostrikov, K. (2019b). Cancer-Targeting Graphene Quantum Dots: Fluorescence Quantum Yields, Stability, and Cell Selectivity. *Adv. Funct. Mater.* **29**, 1805860.
- Zhang, L., Jin, Z., Huang, S., Huang, X., Xu, B., Hu, L., Cui, H., Ruan, S., and Zeng, Y.-J. (2019a). Bio-inspired carbon doped graphitic carbon nitride with booming photocatalytic hydrogen evolution. *Appl. Catal. B Environ.* **246**, 61–71.

iScience, Volume 23

Supplemental Information

Detecting Ferric Iron by Microalgal Residue-Derived Fluorescent Nanosensor with an Advanced Kinetic Model

Feiyu Liu, Shishu Zhu, Deyang Li, Guanying Chen, and Shih-Hsin Ho

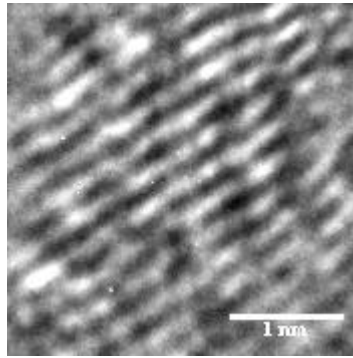


Fig. S1. High resolution TEM image of single CQD (The scale bar is 1.5cm long),

Related to Figure 1.

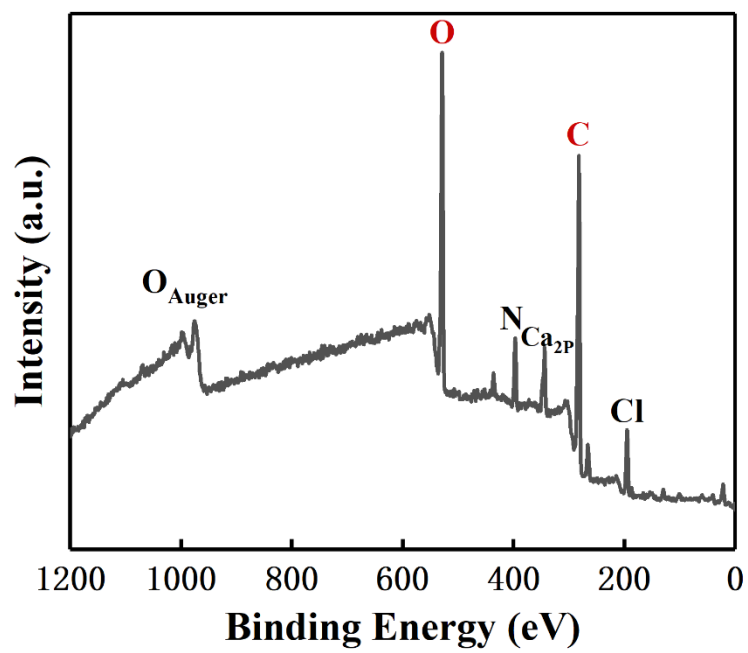


Fig. S2. XPS spectra of CQDs, Related to Figure 1.

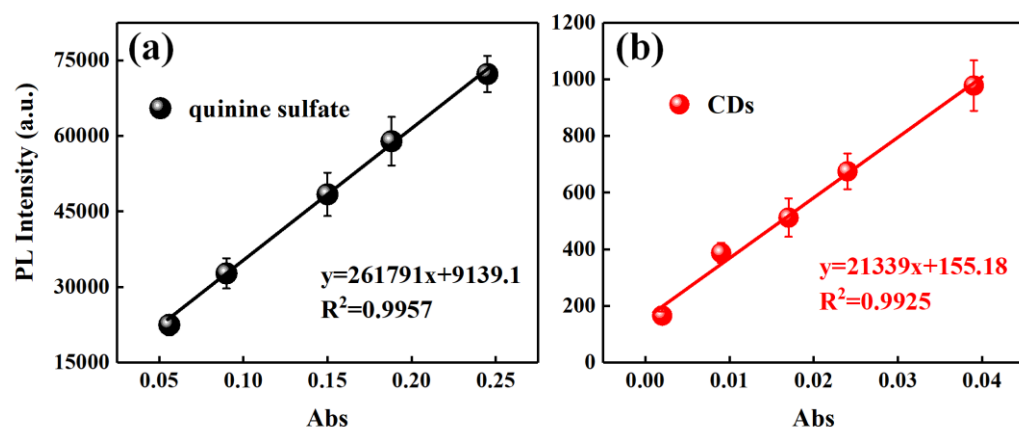


Fig. S3. PL intensity-concentration linear fitting, Related to Figure 2. (a) quinine sulfate.

(b) CQDs.

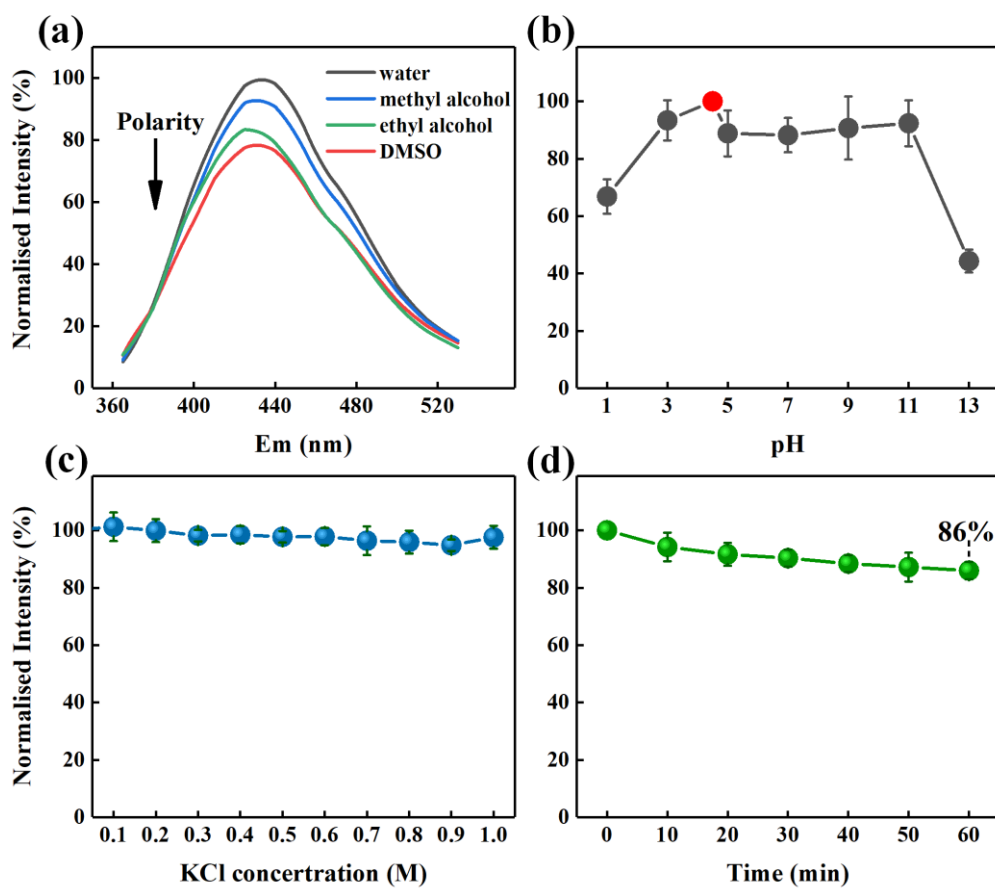


Fig. S4. PL stability, Related to Figure 2. (a) different solvent. (b) pH 1-13. (c) 0.1-1M ions strength. (d) one hour ultraviolet irradiation

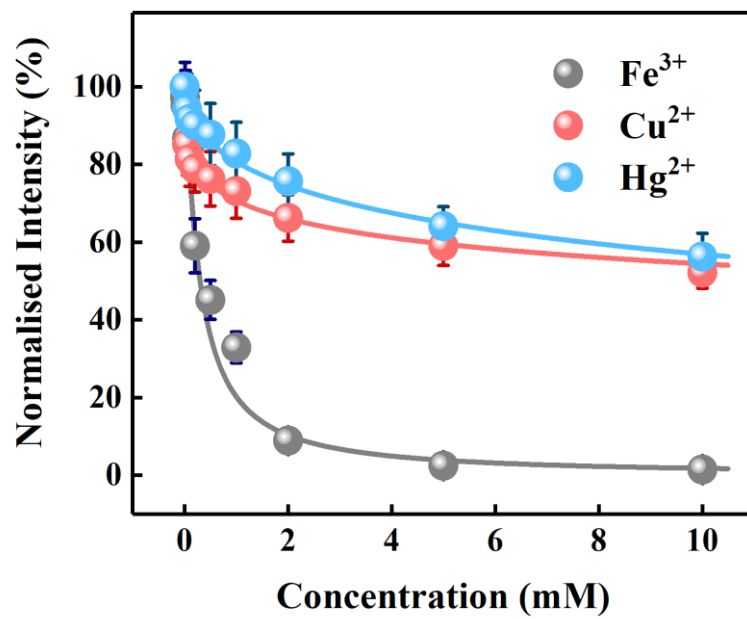


Fig. S5. Kinetic fitting of Fe³⁺, Cu²⁺ and Hg²⁺ quenched CQDs, Related to Figure 3.

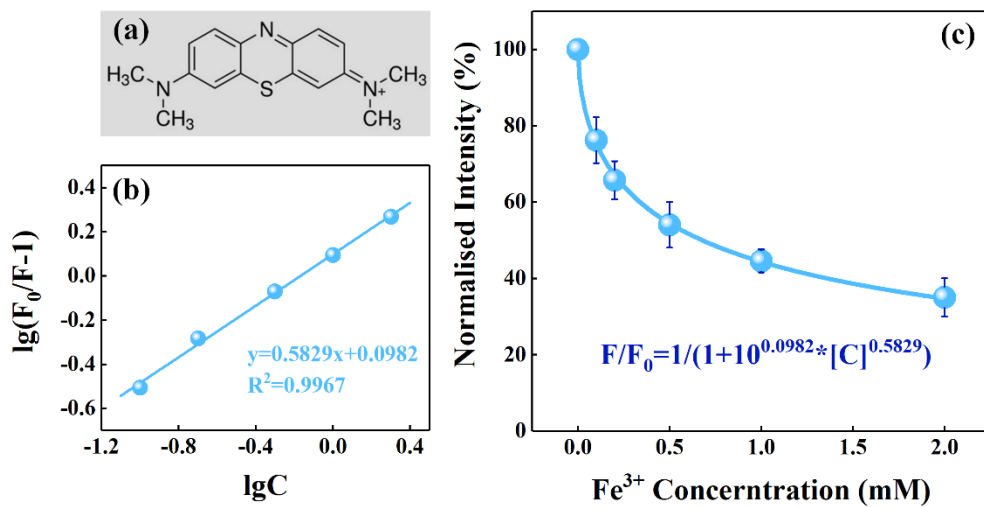


Fig. S6. Application in MB quenching based on multiple order kinetic model, Related to Figure 3. (a) structural formula of methylene blue. (b) coordinate transformation based linear kinetic fitting. (c) kinetic fitting of Fe^{3+} quenched methylene blue.

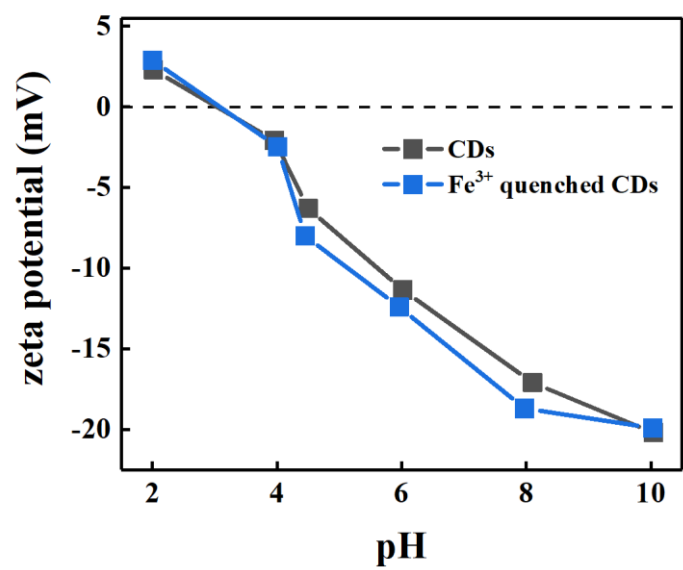


Fig. S7. Zeta potential variation upon pH, Related to Figure 4.

Table S1

Literature review of biomass based CDs fluorescent nanosensor, Related to Figure 3.

CDs precursor	detection object	Kinetic model	Dynamic range	Reference
citric acid	Hg ²⁺	multiple order	0.05-15μM	(Nguyen Thi Ngoc et al., 2017)
<i>Phyllanthus acidus</i>	Fe ³⁺	Partial First order	2-25μM	(Atchudan et al., 2018)
mangosteen pulp	Fe ³⁺	Partial First order	25-280μM	(Yang et al., 2017)
ethylene glycol	humic acid	Two-stage First order	0.01-0.1mg/L 10-50mg/L	(Guan et al., 2017)
Waste Expanded Polystyrene	Au ³⁺	First order	2-18μM	(Ramanan et al., 2018)
citric acid	Hg ²⁺	Two-stage First order	0.001-0.05μM 0.5-5μM	(Ren et al., 2018)
grass	Cu ²⁺	Two-stage First order	0.0005-0.1μM 5-50μM	(Liu et al., 2012)
p-aminosalicylic acid	Fe ³⁺ quench ascorbic acid recover	(Fe ³⁺) First order (ascorbic acid) linear	(Fe ³⁺) 0.05-10μM (ascorbic acid) 0.2-11μM	(Shamsipur et al., 2018)
Microalgae biochar	Pb ²⁺ , Cu ²⁺ , Ni ²⁺	multiple order	(Pb ²⁺) 0.012-5μM (Cu ²⁺) 1-10μM (Ni ²⁺) 0.0125-50μM	(Plácido et al., 2019)

Table S2

Parameters of different quenching system, Related to Figure 3.

Fluorescent source	quencher	$K_{SV}(\text{L}\cdot\text{mol}^{-1})$	i
	Fe^{3+}	3.94×10^3	1.14
CDs	Cu^{2+}	4.2×10^2	0.30
	Hg^{2+}	2.4×10^2	0.49
methylene blue	Fe^{3+}	1.26×10^3	0.58

TRANSPARENT METHODS

Chemicals and Materials. Citric acid (CA), edetic acid (EDTA), methyl alcohol, ethyl alcohol, acetone, dimethyl sulfoxide (DMSO), NaOH, HCl, NaNO₃, Na₂CO₃, Na₂SO₄, NaI, NaCl, KCl, NH₄Cl, CrCl₃, ZnCl₂, MnCl₂, MgCl₂, HgCl₂, FeCl₃, FeCl₂, CuCl₂, CdCl₂, BaCl₂ and NH₃·H₂O were purchased from Sinopharm Chemical Reagent Co., China. Methylene blue (MB) and quinine sulfate were purchased from Aladdin Co., China. All the chemicals were analytical grade and used as received without further purification. Phycocyanin was extracted out of *Spirulina* through commercial operation process while the residues were used as the raw material for CQDs synthesis. Briefly, 50 kg dry *Spirulina* powder and 1200 kg water were mixed for extraction. During the mixing, the temperature was controlled below 18°C with additions of 20-30 kg calcium chloride, 3-5 kg citric acid, and 20 mL sodium hypochlorite. The mixture was initially stirred for 3-5 h and then maintained for 8 h, followed by addition of 15-20 kg of disodium hydrogen phosphate and consequent stirring for another 12 h to yield phycocyanin and *Spirulina* residue.

Synthesis of Carbon Quantum Dots. The CQDs were synthesized by means of a modified hydrothermal method reported by Ramanan et al. (Ramanan et al., 2016). Briefly, 2 g microalgal residue and 40 mL ultrapure water were placed into a 100 mL poly-(tetra-fluoroethylene) (Teflon)-lined autoclave and heated at 150°C for 12 h. After

water-cooling to room temperature, the solid-liquid mixture was centrifuged at 10000 rpm for 15 min and the resultant was filtered through a 0.22 μm membrane. The obtained orange transparent solution was extracted with acetone to remove the hydrophobic by-products. The extracted solution was collected and freeze-dried to obtain solid CQDs with a yield of approximately 30-35 wt %. Desired amounts of obtained CQDs were re-dissolved in deionized water and used for further studies.

Characterization. The size and morphology of the CQDs were characterized by a Transmission electron microscope (TEM, JEOL-2100, JEOL Ltd., Japan) at an acceleration voltage of 200 kV. Fourier transform infrared spectroscopy (FTIR, SPECTRUM one, PerkinElmer, USA) was used to identify the functional groups on the surface of CQDs within the wavenumber region of 400-4000 cm^{-1} . X-ray powder diffraction (XRD, X'PERT Rro MPD, Panalytical, Holland) was used to examine the crystallinity of CQDs over a 2θ collection range of 10-80°. X-ray photoelectron spectroscopy (XPS, ESCA Lab 250Xi, Thermo Fisher Scientific, USA) was performed to examine the surface compositions of CQDs up to a depth of <10 nm. Optical absorption spectra were recorded on a UV-3600 (Shimadzu, Japan) spectrometer. The fluorescence spectra and fluorescence decay measurements were carried out on a spectrofluorimeter (FLS 1000, Edinburgh). To eliminate the concentration-fluorescence intensity effect, the QY of the CQDs was calculated by the equation:

$$\Phi = \Phi_{\text{ref}} \frac{k}{k_{\text{ref}}} \left(\frac{n}{n_{\text{ref}}} \right)^2 \quad (1)$$

where n is the refractive index of solvent, k is the slope of integrated emission intensity-absorbance linear-regression curve under different concentrations, and Φ is the value of QY. The subscript *ref* refers to a standard with known QY, which in this work is quinine sulfate in 0.1 M H₂SO₄ (QY 54% at 360 nm excitation). The software for making figures is Origin 2017.

Fluorescence Quenching of CQDs. The solid-state CQDs were dispersed in deionized water and diluted up to 100 mg/L for application as the probe. For comparison, different metal cations and sodium salts of different anion were added to the probe as solutions with a final concentration of 1 mM. After that, the mixture was blended for 30 s and followed by recording the emissive spectrum at an excitation wavelength of 355 nm. Following the exact process, the CQDs solutions were spiked with Fe(III) at different concentration levels for measuring the emissive spectra to obtain the standard curve. To evaluate the performance of CQDs-based nanosensor for Fe(III) detection by fluorescent quenching-based method in real-water, samples were taken from Songhua River, Harbin, Heilongjiang, China, municipal wastewater from Taiping municipal wastewater treatment plant, Harbin, Heilongjiang, China, and city tap water. The real-water samples were centrifuged at 10,000 rpm for 15 min and then filtered through a 0.22 μm membrane. (Zhang & Chen, 2014) The resultant water samples were spiked

with Fe(III) ions at different concentration levels for analysis.

Kinetic Model of CQDs Quenching. Photoluminescence(PL) quenched by ions were analyzed by dynamic quenching theories(Liang et al., 2016). The correlation between PL intensity and ions concentration was fitted by the SV equation:

$$F_0/F - 1 = K_{SV} [Q] = k_q \tau_0 [Q] \quad (2)$$

where F_0 and F respectively, are the fluorescence intensities in the absence and presence of the quencher; K_{SV} is the Stern–Volmer quenching constant; $[Q]$ is the concentration of the quencher; k_q is the quenching rate-constant and τ_0 is the fluorescence lifetime of the CQDs.

The SV equation was obtained through the following steps:

$$d[M_0^*]/dt = I - (k_f + \sum k_i)[M_0^*] = 0 \quad (3)$$

$$d[M^*]/dt = I - (k_f + \sum k_i + k_q [Q])[M^*] = 0 \quad (4)$$

$$F_0/F = k_f [M_0^*]/k_f [M^*] = (k_f + \sum k_i + k_q [Q]) / (k_f + \sum k_i) = 1 + K_{SV} [Q] \quad (5)$$

where M_0^* and M^* are the number of excited electrons in the absence and presence of quencher, respectively; I is the absorption rate; k_f is the fluorescence-emission rate; $\sum k_i$ is the summation of all the non-radiative jump rates. The SV equation is based on the

assumption that the correlation between the gradient of excited electrons and the concentration of quencher is of first order. In the CQDs-metal ions quenching experiments, however, the kinetic effects were typically partial first-order or two-stage first-order.(Atchudan et al., 2018; Liu et al., 2012) In this study, the multiple order kinetic model was established to describe the quenching process by introducing the parameter of reaction order in the equations. The kinetic equation was inferred from the following steps:

$$d[M^*]/dt = I - (k_f + \sum k_i + k_q [Q]^i)[M^*] = 0 \quad (6)$$

$$\lg(F_0/F - 1) = \lg \left[\frac{k_q [Q]^i}{k_f + \sum k_i} \right] = \lg K_{sv} + i \lg [Q] \quad (7)$$

where i is the reaction order determined by the sizes of CQDs and quencher, the strength of the interaction force and the spectral overlap. By transformation of coordinates and the corresponding fitting, the kinetic curve was obtained which firmly established the detection method according to the standard curve.

Supplemental Reference:

- Atchudan, R., Edison, T.N.J.I., Aseer, K.R., Perumal, S., Karthik, N., Lee, Y.R. 2018. *Biosensors & Bioelectronics*, 99, 303-311.
- Guan, Y.-F., Huang, B.-C., Qian, C., Yu, H.-Q. 2017. *Environmental Science & Technology*, 51(24), 14092-14099.
- Liang, Z., Kang, M., Payne, G.F., Wang, X., Sun, R. 2016. *Acs Applied Materials & Interfaces*, 8(27), 17478-17488.
- Liu, S., Tian, J., Wang, L., Zhang, Y., Qin, X., Luo, Y., Asiri, A.M., Al-Youbi, A.O., Sun, X. 2012. *Advanced Materials*, 24(15), 2037-2041.
- Nguyen Thi Ngoc, A., Chowdhury, A.D., Doong, R.-a. 2017. *Sensors and Actuators B-Chemical*, 252, 1169-1178.
- Plácido, J., Bustamante-López, S., Meissner, K.E., Kelly, D.E., Kelly, S.L. 2019. *Science of The Total Environment*, 656, 531-539.
- Ramanan, V., Siddaiah, B., Raji, K., Ramamurthy, P. 2018. *Acs Sustainable Chemistry & Engineering*, 6(2), 1627-1638.
- Ramanan, V., Thiyagarajan, S.K., Raji, K., Suresh, R., Sekar, R., Ramamurthy, P. 2016. *ACS Sustainable Chemistry & Engineering*, 4(9), 4724-4731.
- Ren, G., Meng, Y., Zhang, Q., Tang, M., Zhu, B., Chai, F., Wang, C., Su, Z. 2018. *New Journal of Chemistry*, 42(9), 6824-6830.
- Shamsipur, M., Molaie, K., Molaabasi, F., Alipour, M., Alizadeh, N., Hosseinkhani, S., Hosseini, M. 2018. *Talanta*, 183, 122-130.
- Yang, R., Guo, X., Jia, L., Zhang, Y., Zhao, Z., Lonshakov, F. 2017. *Applied Surface Science*, 423, 426-432.
- Zhang, R., Chen, W. 2014. *Biosensors & Bioelectronics*, 55, 83-90.